Characterization of a circular arc electron source for a self-neutralizing air-breathing plasma thruster

Anmol Taploo[1,2*], Vikas Soni[1,2], Halen Solomon[2], Marshall McCraw[2], Li Lin[1,2*], Jake Spinelli[1,2], Steven P. Shepard[3], Santiago D. Solares[2] and Michael Keidar[1,2*]

*Correspondence:
anmol035@gwu.edu; lilin@gwu.edu; keidar@gwu.edu

[1] Micro Propulsion and Nanotechnology Laboratory, George Washington University, Washington, DC 20052, USA
[2] Department of Mechanical and Aerospace Engineering, George Washington University, Washington, DC 20052, USA
[3] Research Programs: Power and Propulsion, Counter Directed Energy, Lockheed Martin, Palo Alto, CA 94304, USA

Abstract

The paper presents an enhanced version of an arc electron source designed for air ionization applications in a self-neutralizing air-breathing plasma thruster. The arc electron source is specifically suited for the air-breathing plasma thruster, as it allows precise control of mean electron energy levels. This paper focuses on the ionization aspects of air-breathing thrusters through the development of axially magnetized arc electron sources. The sources consist of a circular and coaxial configuration of a metallic arc plasma source coupled with a positively biased grid to extract electrons and control mean electron energy. The average mean electron energy of electrons in the arc electron source is regulated by adjusting the bias voltage of the grid within the range of 0 V – 300 V. To investigate the behavior of ion current density and electron density concerning pressure and mean electron energy, the current probe and magnetic filter were utilized. It was demonstrated that the circular electron source leads to enhanced ionization of airflow by achieving plasma densities greater than 10^{18} m^{-3}. By utilizing a high-speed camera for the circular arc electron source, the arc spot was seen to move azimuthally due to the magnetic field. Furthermore, scanning electron microscopy and a conductance measurement system were employed for the coaxial arc electron source to examine the deposition and conductance of the electron extraction grid. While the grid underwent deposition of about 600 microns, the conductance was observed to increase/saturate with time and bias voltage, indicating an electrically "self-healing material".

Keywords: Air-breathing, High-Speed Camera, Deposition, Self-Healing Material, Neutralization

Introduction

Very low earth orbits (VLEOs) have been an area of interest for a long time. Recently the research and development of air-breathing plasma propulsion devices in VLEOs (80 km to 260 km) have been surging [1–4]. To effectively counteract drag levels ranging from 60 mN to 60 N within VLEOs, a minimum thrust level equivalent to or greater than the norm is necessary [1, 2]. Enhanced satellite mission capabilities, such as (i) earth imaging, (ii) reduced atmospheric pollution, (iii) decoupled propellant storage (resulting in

lower launch costs), (iv) extended lifetime [5], and (iv) prevention of space debris forma-tion [1], are among the advantages attributed to operating in low earth orbits. Generally, plasma thrusters that utilize air for propulsion include an air collimator, like a honey-comb structure, to gather and compress incoming air particles. However, challenges arise from the inefficient collimator air inlet design and compression of incoming air leading to excessive drag that exceeds the thrust [2]. Additionally, the power require-ments for the system are exorbitant [1], posing further difficulties. Moreover, there is a need to develop effective methods to enhance ionization for air-breathing plasma thrust-ers, which is currently lacking.

Previously, we proposed a scramjet-type air collimation-less design [1, 2, 4] for an air-breathing plasma thruster. In a scramjet-type inlet design, the incoming air is at a high speed that is not de-accelerated. Commonly, a plasma thruster would be neutral-ized using an external cathode electron injector downstream (to achieve neutralization with ion beam downstream) that would require a separate gas flow tank and increase the thruster weight. However, we hypothesize a simplified neutralizer-less design, i.e., a self-neutralizing air-breathing plasma thruster (SABPT), which would utilize negative and positive ions of air plasma to achieve self-neutralization [1, 2]. Bi-polarity ions could be extracted using applied alternating electric fields between charge extraction electrodes, so charge densities would nullify to create a neutralized jet. The plasma generation in SABPT was previously suggested [2] using an arc electron source (AES) coaxial configu-ration with eminent control over its mean electron energy for ion formation. Coaxial AES [2] comprises a coaxial vacuum arc-based source coupled with an electron extrac-tion grid. The electrons generated in the arc plasma are extracted using a grid biased positively. The high and low energy modes of the AES would result in the creation of positive and negative ions subsequently. AES operation would require the production of high-density plasma in harsh air plasma environments. The axial plasma generated by coaxial AES requires multiple designs placed around its circumference to ionize incom-ing air effectively (that would increase the required power). While AES produces arc plasma, electrons are extracted from the plasma and not through surface emission. As such this electron source is expected to have a longer lifetime. Consequently, we present an alternate improved version of a low-power AES as an electron source for air ioniza-tion in a circular configuration for SABPT.

Substantial research has been done on vacuum arcs using various cathode materials since the nineteenth century [2, 6]. Researchers have used magnetic fields to enhance the vacuum arc's plasma parameters such as density, electron temperature, and ion and electron current [1, 2, 6, 7]. For thruster applications [8, 9], vacuum arcs have shown multimodality [10] and promising results in terms of achieving over two million pulses [11] during their operation. Additionally, vacuum arcs for electron source applications have shown the formation of ions of both polarities [2] in an air plasma at a medium pressure range. Recently, researchers have reported the use of positive and negative ions for achieving neutralization [2, 12–16]. A grid RF thruster built by Aanesland et al. [12] created a high ion-ion plasma density downstream of a magnetic filter (due to low elec-tron temperature) and individual charges were accelerated using a ± 400 V electric field in kHz frequency to achieve neutralization. To identify positive and negative ions down-stream for neutralization, Gerst et al. [13] built an $E \times B$ probe for a sulfur hexafluoride

plasma. Additionally, the authors [12, 13] have emphasized that the high recombination rate of electronegative gas plasma downstream results in neutralization. The designs mentioned above were built and tested with electronegative gases, but not using air. Earlier, we showed that a vacuum arc-based coaxial electron source can create both positive and negative ions in air plasma [2]. However multiple sources would be required for SABPT's cylindrical geometry. Hence, we propose a circular arc electron source (CAES) for SABPT. CAES has innumerable advantages such as ease of manufacturing, long lifetime, operability in harsh plasma environments (vacuum-medium pressure range), not requiring a separate gas flow, utilization of its cathode as a plasma source, and stable operation in pulsed regime while utilizing less input power (about an average of 0.15 W/A per pulse for discharge voltage and current as 1200 V and 33A). In summary, CAES air ionization with self-neutralization capabilities for SABPT can be incorporated to avoid propellant storage and complicated designs.

As previously proposed, CAES requires eminent control over mean electron energy to be used as a suitable electron source to ionize air inside SABPT. Consequently, CAES is equipped with an electron extraction grid (Fig. 1). The positive bias on the grid results in the radial direction extraction of electrons from the vacuum arc plasma, unlike AES [2]. The increment of mean electron energy is directly proportional to the increase in the bias. The high and low energy operation would form positive and negative ions (dissociative electron attachment [17]). Although the
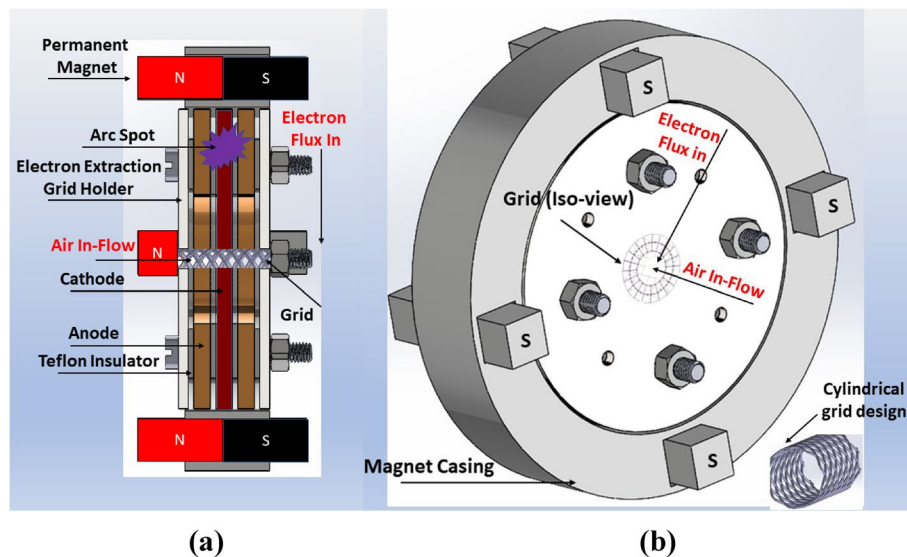

(a)   **(b)**

Fig. 1 **a** and **b** Schematics of a CAES show the vacuum arc plasma source comprising the cathode, anode, permanent magnets, grid holder, aluminum grid, magnet casing, and Teflon insulators. A highly concentrated electric field forms between the gaps to initiate a cathode spot [2, 19]. **b** The image shows the placement of a cylindrical electron extraction aluminum grid in the vicinity of the source. The flexible cylindrical grid can be seen. The grid was placed inside the central aperture of the CAES. The direction of air inflow and electron flux is depicted in Fig. 1. The mean electron energy of the extracted electrons is controlled by varying the electric potential of the grid. The electrons are removed radially due to the electric field formed between the vacuum arc source and the grid. The permanent magnets are used to generate an axial magnetic field for CAES. Although direct observation of the actual arc spot is not feasible, a schematic is used to determine the location of the arc spot (shown in purple), which is positioned between the two anodes at the cathode interface

electron current depends on electron drift velocity (direct proportionality), electron extraction can be disrupted (by arcing) due to operational proximity with the Paschen curve [18] at very high voltages and pressures. The increment in mean electron energy results in intensified collisions with neutral air atoms, thereby causing ionization. The ionization rate (electron density/neutral density) improves with the grid voltage (mean electron energy) according to the observation in [1]. Simultaneously, at lower energies (less than 4 V), O^- ion density is more substantial than positive charge density as the attachment reaction dominates the ionization rate coefficient [1]. The chemistry model outlined in [1] originates from 0-D simulations. Its primary objective involved examining plasma chemistry within extremely low Earth orbits (80–110 km) and evaluating the feasibility of SABPT for potential flight. As energy levels escalated, notable elevations in ionization densities were identified, akin to the outcomes seen in plasma generated utilizing an arc electron source. Furthermore, simulation outcomes also illustrated that lower energy levels (1–5 eV) led to the generation of heightened negative ion densities, whereas higher energy levels (> 5 eV) resulted in elevated positive ion densities. These outcomes were confirmed by experimental observations [2].

The schematics of CAES are shown in Fig. 1. The design (Fig. 1) shows the magnet casing, two anodes, one cathode, four Teflon insulators, an aluminum grid, a grid holder, and four permanent magnets oriented at 90° from each other. The cathode spot is generated between two anodes and two Teflon insulators (for electric field symmetry) on the interface of the cathode. The spot generation mechanism consists of electron emission, ionization, and charge diffusion. A small portion of ions returns to the surface after ionization, causing heating and generation of cathode spots. Traditionally, ion current amounts to less than 10% of the arc, whereas the remaining is the electron current [20]. Therefore, CAES is built to utilize the unused electrons from the arc. Later, we prove that the CAES can also generate greater plasma densities as compared to coaxial AES [2].

This paper characterizes CAES and coaxial AES [2] for air ionization applications in SABPT. The experimental data presented here describe the generation of ions, the compression effect of pressure, the range of CAES operational parameters on the cathode spot, and studies deposition on the aluminum grid material. Diagnostics tools used to characterize the CAES, and the air plasma include the current probe, magnetic filter, intensified charged coupled device (ICCD) camera analysis, scanning electron microscope (SEM), and conductance measurement system (CMS). The current probe was used to obtain positive ion current density and electron density as a function of pressure and mean electron energy. The magnetic filter was utilized to obtain the peak negative ion current density. The ICCD camera analysis was used to visualize the effect of external parameters such as operating frequency, arc voltage, the pulse width of the power-providing unit (PPU), and the pressure on the cathode spot of the CAES (without any electron extraction). Lastly, SEM and CMS were used to study deposition on the electron extraction grid and measure its conductance, as a function of grid voltage and plasma treatment time.

Experimental setup and diagnostics

The primary focus of this paper is to characterize CAES for air ionization. Figure 1 shows a vacuum arc source, copper electrodes, and Teflon insulator rings. The cathode spot is formed on the cathode and insulator between the two anodes. This cathode spot can rotate under the influence of an axial magnetic field in J (current density) × B (magnetic field) motion [2, 8]. Additionally, to prevent surface barrier discharge between the anode and grid at higher voltages, Teflon rings were added (Fig. 1) between the anode and grid holder. The arcing over the surface disrupted the electron extraction.

A complete electron source comprising a circular vacuum arc source and the electron extraction grid can be observed in Fig. 1. The extraction grid is positively biased with respect to the ground [2]. The unsheathed electron current and energy are functions of the applied grid potential. The electron current extracted saturates at some applied voltage. While a typical electron source (hollow cathode) would require a vacuum background, a thermionic emitter heating system, and a separate propellant tank for its application, it is interesting to point out that CAES does not require those systems. Most importantly, CAES can efficiently operate in the medium pressure range (10^{-4} Torr – 10^{-1} Torr) like coaxial AES [2]. The primary goal is to utilize negative ions and positive ions generated through the air ionization process with CAES to achieve an extracted neutralized beam (due to charge cancellation) at the exit of the SABPT [1, 2]. Both negative and positive ions will be accelerated by appropriate electric field arrangements and by switching the electrodes' polarity [1, 2].

This paper describes CAES using intrusive and non-intrusive plasma diagnostics methods. Figure 2a and b shows the system design configuration starting with a PPU inductive energy storage circuit [2, 21] to power the AES. The inductance, capacitance, switch, input DC voltage, PWM (pulse width modulation) width, frequency, and coil magnetic field values at the arc interface were 550 µH, 6800 µF, IXYH50N120C3D1 IGBT, 18–30 V, 610–1020 µs, 1–10 Hz, and 0.035 T, respectively. The input 5 V pulse to the gate was provided using an Agilent Waveform generator model 33220A [22]. The resistance between the two anodes and the cathode was approximately 100–200 Ω. During stage 1, the IGBT gate was closed, and a high emf was generated in the inductor as it charged.

The gate was unlatched in the second stage, and the stored inductor energy was dispensed into the vacuum arc source. With the addition of a capacitor, the overall discharge current was increased. The inner and outer diameter, and height dimensions for the cylindrical electrodes (anode and cathode) and Teflon are (40 mm, 90 mm, and 6 mm) and (40 mm, 76 mm, and 1.5 mm), respectively. These dimensions were chosen tentatively as our primary focus is studying ionization and optimization. The ceramic was thin enough to create a good conduction gap and required a thin carbon paint layer [10, 23] (100 Ω—200 Ω resistance between cathode and anodes for triggerless arcing) to ignite the arc. The electron extraction grid is an aluminum grid aperture (diameter 4 mm for each opening) placed in a 3D printed grid holder with inner and outer diameters and heights of 13 mm, 90 mm, and 3 mm, respectively. The aperture was 14.5 mm away from the source to avoid arcing. The chamber was pumped down using a roughing pump to reach a base pressure of 0.05 Torr. An air leak allowed for a small air flow rate into the chamber. A current probe with a 37 mm wire length was placed inside the plasma area
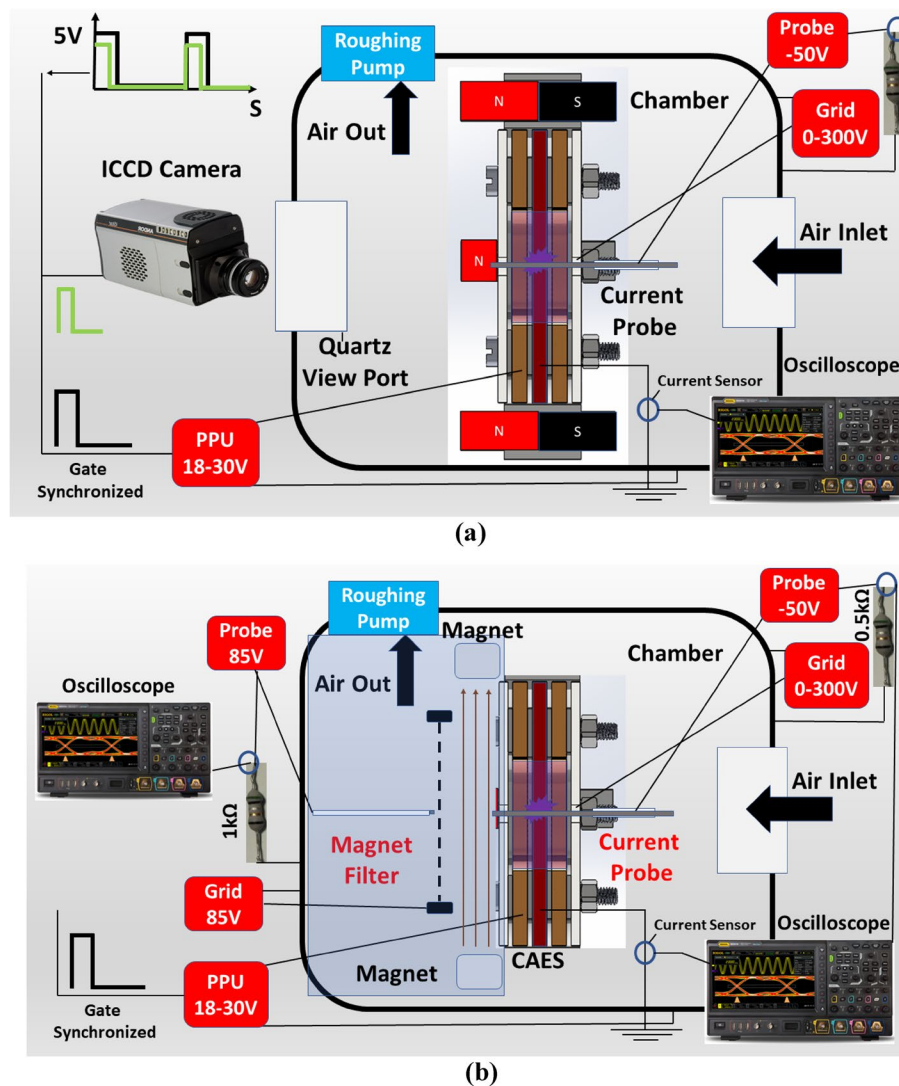
Fig. 2 Schematics of the plasma diagnostics for CAES. **a** The diagnostics method for ICCD camera analysis is displayed. The distance between the electron extraction grid and the vacuum arc source was 13 mm. **b** Simultaneously, ion current density was measured using a current probe, and negative ion current density (blue region) was measured using a magnetic filter (similar concept as described previously [2]), as shown. To measure positive ion current density, the current probe was biased to −50 V. The current probe was at the center of the AES (20 mm from the cathode and 7 mm from the grid). Additionally, to measure negative ion current density, the Langmuir probe and the charge extraction grid were biased to +85 V. Four permanent magnets were used to axially confine electrons. Probe voltages were set up to measure saturated current. The signals were obtained through oscilloscopes. The plasma chamber was grounded for all experiments. The PPU circuit is an inductive energy storage circuit that is the same as described in Fig. 2 of [2]

(Fig. 2b) for positive ion current density and electron density probe experiments. The measurement circuit for the probe is shown in Fig. 2b. Simultaneously, Fig. 2b shows a schematic of the magnetic filter for negative ion current density measurements. A combination of axial magnetic field (N42 bar magnets with maximum remanent magnetic flux 1.35 T), charge extraction grid (diameter 10 cm), and Langmuir probe (2 mm wire length) were utilized. For ICCD camera analysis, an Andor iSTAR 334 T [24] was placed with a zoom lens close to the quartz viewing port of the chamber to focus on the

CAES. The camera was covered with a black cloth to cancel out the background optical noise. The vendor provided Andor Solis software, which was used on a PC to obtain high-speed images of the arc spot. The details about SEM and CMS are mentioned in Sect. "SEM and conductance measurements".
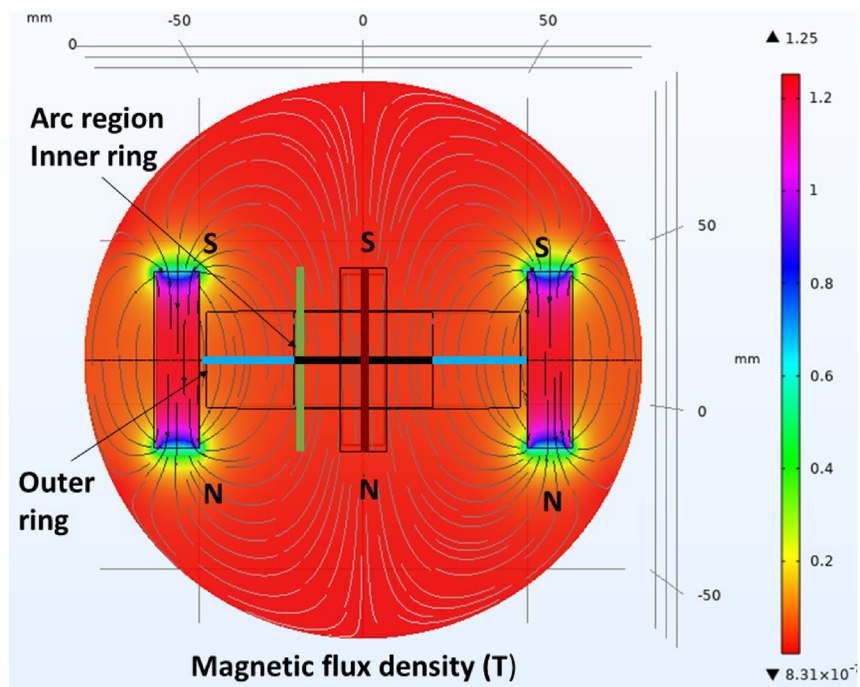
Addition of axial magnetic field

To improve the performance of the source, we added an integrated air-cored coil axial magnetic field of 0.15 T [2] for a coaxial AES configuration, to create cathode spot rotation [2, 8] and uniform cathode erosion at the cathode insulator. Additionally, the direction of the current was parallel to the axial magnetic field. In contrast, in CAES we have created an axial magnetic field parallel to the axial current direction using four Neodymium N42 permanent magnets, as shown in Figs. 1, 2 and 3. Figure 3b shows that around 0.035 T of the magnetic field was applied at the arc interface annotated as the "inner circle".
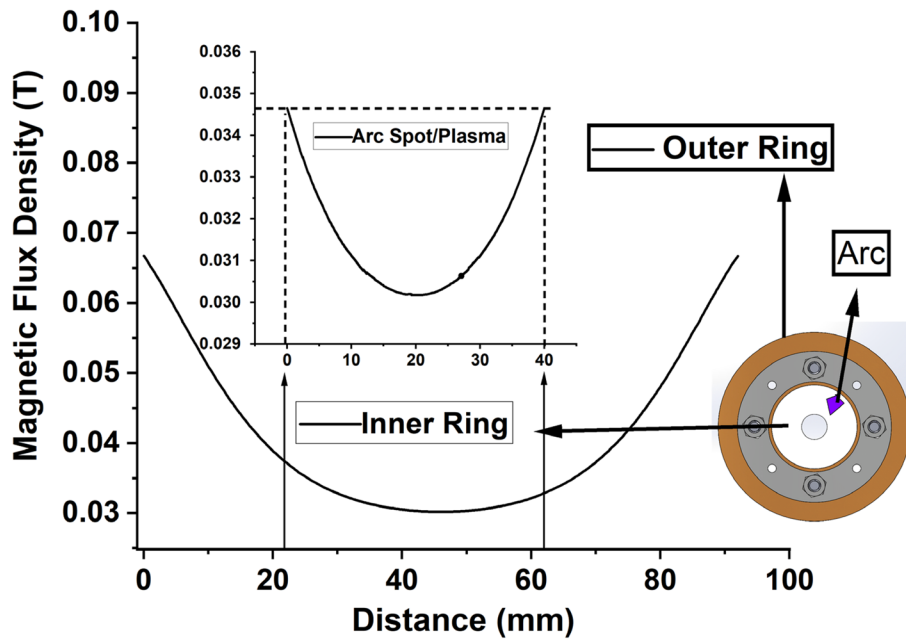
The magnetic field generated by permanent magnets was simulated in COMSOL [25], as shown in Fig. 3a and b. A 3D time-invariant field equations model was simulated with input conditions of N42 magnet dimensions and distance from the center as 12.7 mm $\times$ 12.7 mm and 46 mm, respectively. For the simulation, the magnetization input was assigned to the model as a B-H demagnetization curve data, obtained from K&J Magnetics for an N42 grade permanent magnet [26]. Figure 3b shows the magnetic flux density profile between two magnets shown by the blue and black line in Fig. 3a. A peak magnetic field of around 0.035 T can be seen at the interface of the arc spot in Fig. 3b. The magnified plot shows the magnetic flux density in the inner circle region (arc /plasma area). The difference in the magnetic field leads to an increase in electron transport to the center of the CAES. Consequently, because of increased collisions, the addition of the proposed magnetic field configuration would potentially lead to an improved CAES in comparison with coaxial AES [2]. In this work, the effect of the magnetic field applied on the cathode, as well as the corresponding spot dynamics was studied using an ICCD camera.

Current probe and magnetic filter measurements

A current probe having an area of 5.89×10^{-5} m^2 was utilized. The current was calculated for a potential drop across a 500 Ω resistor. The current probe was built with titanium wire for a thickness and length of 0.5 mm, and 37 mm, respectively, exposed to plasma (the remaining current probe was shielded using a non-porous alumina ceramic). The procedure involves obtaining the saturated ion current and using the ion saturation current equation. The electron density was obtained by keeping the electron temperature at around 1 eV which is typical for vacuum arc sources. Earlier we obtained electron temperature in the 1–2 eV range for coaxial AES described in [2]. It was obtained through an I-V curve using a Langmuir probe. Simultaneously, peak negative ion current measurements were performed using a magnet filter using a charge extraction grid, N42 magnets for electron confinement using axial magnetic field, and a Langmuir probe. This is a similar concept as previously described [2]. The Langmuir probe results reveal two distinct current peaks concerning the filter. The initial peak signifies the electrons that have managed to evade the magnetic filter, whereas the subsequent peak is

(a)

(b)

Fig. 3 a COMSOL magnetic fields – no current module was solved for N42 permanent magnets, magnetic flux density (T) variation with the distance between two magnets annotated by the blue and black line. **b** An axial magnetic field component profile can be seen where the inner ring is the area of arc and air plasma generation

representative of the negative ion current. The function of the filter is to confine electrons owing to their relatively small Larmor radius, whereas it permits negative ions to traverse through due to their Larmor radius surpassing the source length. Additionally, a grid was employed to extract negative ions from the air plasma. The results have been presented in Sect. "Plasma parameters".

ICCD high-speed camera experiments

An ICCD camera operates based on intensification and light detection. In essence, an ICCD camera comprises a standard CCD sensor coupled with an image intensifier. The cathode spot generation in an arc source has been an area of interest. Consequently, researchers have also attempted to study this effect at the nano- to millisecond scale using ICCD high-speed imaging cameras. For instance, Methling et al. used the ICCD camera's accumulation mode in a nanosecond regime [27] to achieve improved sensitivity and signal-to-noise ratio for recording data on the dynamics of spectral line radiation generated by a Ga-In cathode-based vacuum discharge. For a copper cathode-based vacuum arc, Burkhard [28] used an ICCD camera consisting of framing and streak channels to achieve a spatial and temporal resolution of arc spots in the 200–800 nm spectral range. Subsequently, the effect on the cathode spot due to the magnetic field was studied using an ICCD camera for Argon plasmas. For instance, the rotation of cathode spots was observed by Dong et al. [29]. Additionally, Wang et. al. [30] investigated the variation of cathode spot rotation velocity, erosion rate, and qualitative spot diameter under the influence of the magnetic field, gas flow rate, and arc current. While most works were conducted for arc sources in vacuum conditions, the research lacked experimental camera data for medium pressure regimes (for air plasma). Generally, the addition of a magnetic field improves ionization and ion velocities for vacuum arc sources [2, 8].

To this end, we studied a magnetically enhanced CAES for air ionization in a medium-pressure regime using an ICCD high-speed imaging camera. The ICCD camera technique gave an insight into arc spot behavior change as a function of PPU operation (frequency, pulse width, and applied voltage) and plasma chamber pressure under the influence of the axial magnetic field. The high-speed images were captured using Andor Solis software. The camera input pulse (5 V, 20 ns) waveform was synchronized with an Agilent waveform generator using a 50 MHz WAVETEK pulse generator [31]. The camera was set to an internal trigger with continuous wave (CW) mode. Initially, the ICCD camera was aligned in the plane with the front view of the circular arc source (without the grid holder and the aluminum grid) focused using a Nikon Micro-NIKKOR 55 mm f/2.8 lens [32]. Once aligned, the trigger was set to external (input from WAVETEK waveform generator) and the acquisition mode to kinetic. The input for the pixels, delay, TTL/exposure time width, step, and the number of accumulations were set as 1024×1024, CAES's pulse width (620–1020 μs), 1–30 μs, 1 ps, and 30. Lastly, the peak intensities from the images were obtained and processed using an in-house Python script created for this purpose.

SEM and conductance measurements

SEM and CMS were used to study the deposition thickness and conductance of the aluminum electron extraction grid. To evaluate the surface topography of deposits on

the aluminum grid used in this study, we performed SEM of the samples using an FEI Teneo LV SEM instrument (GWNIC, George Washington University [33]) as seen in Fig. 4b. The results have been presented in "Deposition thickness and conductance analysis " section. To study the conductance of the grid, an experiment was built using the previously proposed coaxial AES [2]. It consists of a vacuum arc-based plasma source coupled with an electron extraction grid. The coaxial AES was used instead of CAES to establish a straightforward quick and simple experimental setup for observing the effects of air plasma or harsh plasma conditions on the electron extraction grid. The objective was to study the variation of conductance of the electron extraction aluminum
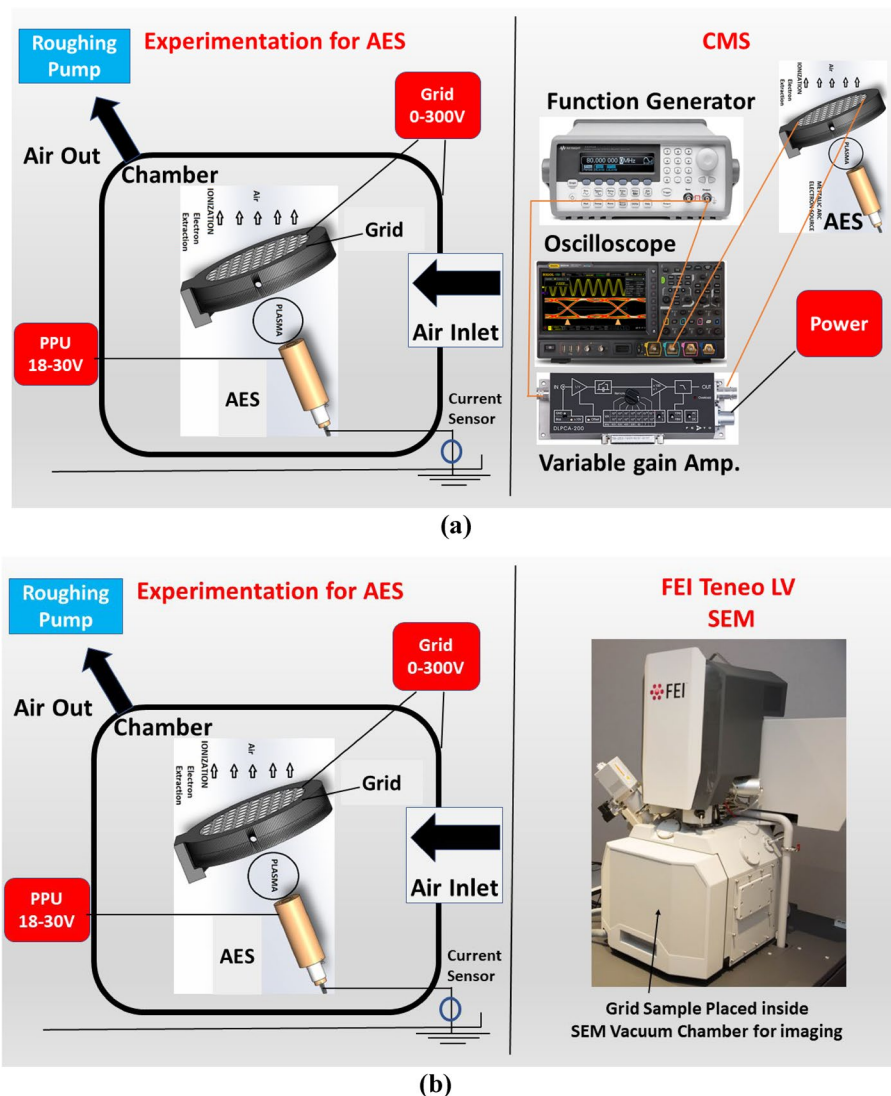

(a)

(b)

Fig. 4 CMS and SEM experiment setup. **a** The figure on the left shows the coaxial AES [2] set up in the vacuum chamber for 20 min at each interval. The setup was removed, and IV characteristics were measured to obtain the conductance of the grid (the CMS setup is shown on the right). The grid for bias 0 and 300 V was treated in the plasma chamber while IV characteristics were measured simultaneously. **b** The figure on the right shows the FEI Teneo LV [33] SEM machine. The grid cut section sample was placed inside its vacuum imaging chamber for analysis. The pressure in the plasma chamber (on left), PPU voltage, pulse width, and frequency were 0.05 Torr, 20 V, 620 μs, and 5 Hz, respectively

Taploo *et al. Journal of Electric Propulsion*   (2023) 2:21

Page 11 of 23

grid as a function of treatment time and grid voltage. Initially, we proposed the hypothesis that the conductance of the grid would potentially rise with exposure to plasma, thereby making the grid an electrically "self-healing material". Possibly the sputtering/erosion of grids can occur over time due to ions from the high ionization degree vacuum arc plasma. Sputtering/erosion of an electron extraction grid reduces its conductance by decreasing the effective surface area for electron flow, increasing resistance. This compromises the efficiency of electron extraction and can lead to a shorter grid lifetime due to degradation and potential failure caused by erosion-induced structural damage. Hence, the conductance and lifetime of the grid are affected.

Additionally, atomic oxygen present in the atmosphere could also lead to oxidation/erosion. While the erosion/drop in conductance is difficult to control, it is interesting to study the parameters responsible for it. We have utilized an experimental approach to study the conductance behavior of the grid in AES using a CMS method (as a function of voltage and treatment time), as described in Fig. 4a. AES [2] in a plasma chamber has been used to simulate VLEO harsh plasma environments. To obtain the conductance, the grid was connected to an arbitrary function generator (Model 33220A KEYSIGHT, Santa Rosa, CA [22]), with a DLPCA-200 variable-gain, low-noise current amplifier (FEMTO, Berlin, Germany [34]) connected in series to the grid assembly (see Fig. 4a). A voltage ramp with an amplitude of 5 V and a frequency of 1 kHz was applied for 30 s to each sample. The variable-gain current amplifier was set to $10^3 \frac{V}{A}$. The output from the current amplifier was then recorded by an SDS 1052DL + oscilloscope (SIGLENT, Solon, OH [35]). Each sample was measured five times to ensure measurement accuracy. The conductance results have been described in "Deposition thickness and conductance analysis " section.

Results

In this section, the results of CAES characterization are presented. Firstly, plasma parameters are presented based on probe measurements, and results are compared with coaxial AES [2]. We show that both positive and negative ions can be formed by varying the grid voltage (mean electron energy) using CAES. Secondly, the effect of the axial magnetic field on the cathode spot was studied as a function of pressure, discharge voltage, discharge frequency, pulse width, and exposure time, using an ICCD camera. Finally, the deposition and fluctuations in conductance resulting from the interaction of the air plasma with the electron extraction grid were examined through the utilization of SEM and CMS. The results are presented below.

Plasma parameters

The maximum positive ion and negative current density as a function of grid voltage/energy are presented in Fig. 5. The experiments indicated that by varying the grid voltage, both positive and negative ions can be created in CAES. A maximum positive and negative ion current density of 810 and 180 Am^{-2}, respectively, (1000 times greater than coaxial AES [2]) at a grid voltage of 300 V and 0 V were obtained, as seen in Fig. 5.

The influence of the arc on both the arc source and the grid had minimal impact on electron extraction, as observed through an average over the pulsed duration. To quantify this effect, the electron current relative to grid voltage and pressure was analyzed
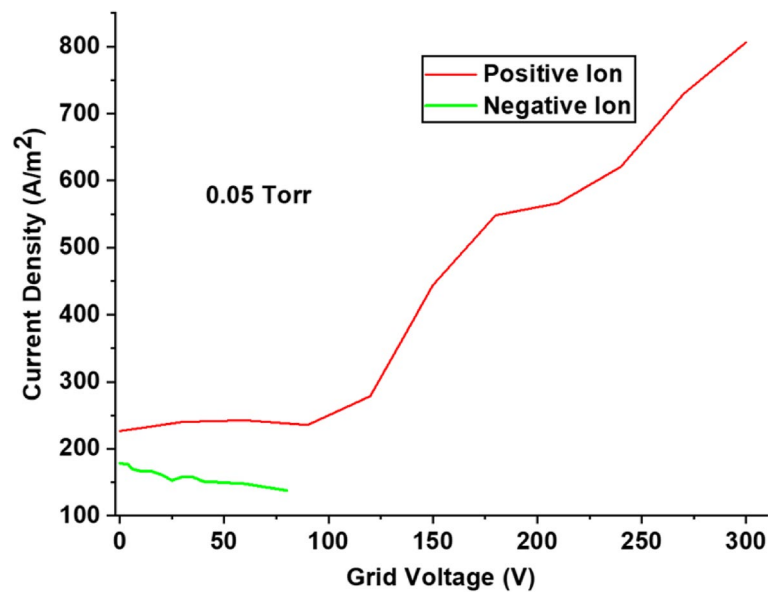
Fig. 5 Variation of positive and negative ion current density with grid voltage at 0.05 Torr. The positive and negative current density measured was the saturated current in the air. The increase in the positive ion current density with grid voltage indicates air ionization, as previously seen [2]. A decrease in the negative ion current density with grid voltage indicates the detachment of electrons. The arc source was operated with PPU voltage, pulse width, and frequency of 20 V, 620 μs, and 5 Hz, respectively

to identify any potential decline or variance in readings over time. Our measurements revealed that electron extraction remained consistent at lower pressures and grid voltages below 300 V. Moreover, we found that increasing the spacing between the grid and the arc source could effectively prevent arcing and secondary electron emission at higher pressure and voltage levels. It's indeed accurate to acknowledge the substantial uncertainty associated with the thin sheath approach in estimating electron density. The values observed in the oscilloscope averaged over 128 values and experiments were repeated 3 times with measurement accuracy greater than 95%. Error bars were intentionally omitted from the electron density plots due to their negligible magnitude, rendering them visually indistinguishable as dots. The radial motion of the electrons enhanced the effective electron impact collisions with the incoming neutral molecules to produce higher positive ion current and lower negative ion current density. For the results presented in this section, the current probe experiments were performed without the presence of external magnetic fields as obtaining the optimum field is currently out of the scope of this research. Nevertheless, the addition of an optimized magnetic field would result in an increase in the ionization degree and effective erosion of the cathode material. Later we also describe the effect of an external magnetic field on the cathode spot.

The current probe was used to obtain positive ion current density as a function of grid voltage and pressure. Consequently, electron density was calculated (procedure described in [2]) using electron temperature (T_e) of 1 eV (1–2 eV is typical for vacuum arc sources [2]). Figure 6b shows the variation of electron density with pressure. The CAES produced 100–1000 times higher electron densities as compared to coaxial AES. The downfall in electron density with pressure for CAES was 10–100 times, whereas for coaxial AES it was 1000–10,000 times. The reduction in electron density indicated
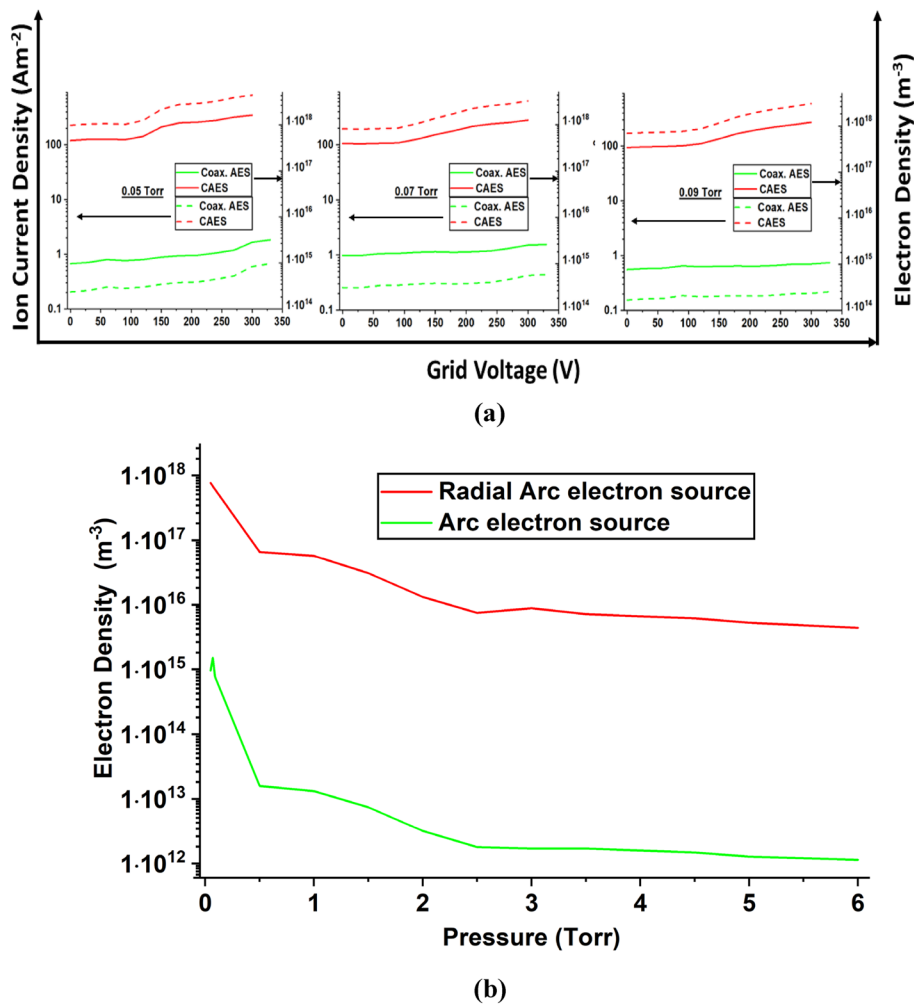
Fig. 6 a The ion current density along with computed electron densities as a function of the extraction grid voltage at pressures 0.05 Torr, 0.07 Torr, and 0.09 Torr, on the Log_{10} scale for CAES can be seen. **b** Additionally, the computed electron density as a function of pressure (0.05–6 Torr) can be seen at a grid voltage of 0 V. The results were compared with earlier coaxial AES experiments [2]. CAES was operated with PPU voltage, pulse width, and frequency of 20 V, 620 μs, and 5 Hz, respectively

ionization of air by CAES over lower volume as compared to coaxial AES. Simultaneously, ion current density (Fig. 6a) can be seen to be 1000 times higher for CAES and increases with the grid voltage. The increase in ion current density can be 3.5 (0.05–0.09 Torr range) times up to 300 V whereas for CAES it is 2.5 times. The maximum positive ion current densities and electron densities corresponding to 0.05, 0.07, and 0.09 Torr pressure were 8.06×10^2 Am^{-2} and 1.62×10^{18} m^{-3}, 6.25×10^2 Am^{-2} and 1.25×10^{18} m^{-3}, 5.93×10^2 Am^{-2} and 1.2×10^{18} m^{-3}, respectively. These conditions were obtained at 300 V grid voltage. At 0.07 Torr and 0.09 Torr, there was airflow into the plasma chamber, whereas 0.05 Torr was the base pressure. The bias of the probe was −50 V as the saturated current was received. The increment in the electron density with grid voltage indicated air ionization. Our earlier results [1, 2] confirmed that the electron densities increased with the mean electron energy as the ionization reaction rate

coefficient is a function of electron temperature. With the increase in the PPU voltage or pulse width, higher plasma current and densities can be achieved as a function of pressure and grid voltage. In the following section, the effects of external parameters on the cathode spot are described.

Arc rotation

ICCD imaging provided an insight into the effect of parameters such as external axial magnetic field, CAES's operating frequency, PPU voltage, pulse width of PPU, and pressure on the cathode spot. The external parameter effects on cathode spot have been imaged and peak emission intensities are presented in this section.

Figure 7 shows the effect of PPU voltage on the cathode spot for various ICCD camera exposure times. The size of the cathode spot appears to be increasing with the camera's exposure time as it allows more emitted photons to enter the detector. The circle shown in Fig. 7 shows the front view of the circular arc source. As observed, a dense plasma is created in the vicinity of the cathode as seen at higher camera exposure times (Fig. 7a). At lower exposure times, the cathode spots will appear to be moving rapidly, thus forming an azimuthally uniform plasma. Although the spots were formed in the inner radius of CAES, the images were taken in the absence of the grid and the grid holder from the CAES assembly. The highest intensity/brightest region indicates the cumulative cathode spots forming a giant spot whereas the lighter area surrounding the spot is the region of air plasma generated by the interaction of the arc with neutral air molecules. In Fig. 7b, an increase in PPU voltage leads to an increment in discharge current. Simultaneously, the distance between cathode spots becomes shorter, which leads to an increment in the mean size/radius of the spot. Multiple spots may form when the arc current exceeds the current that a single spot normally carries. Although the physics of cathode spot formation itself is a much more complicated [36] problem, it was observed that a higher
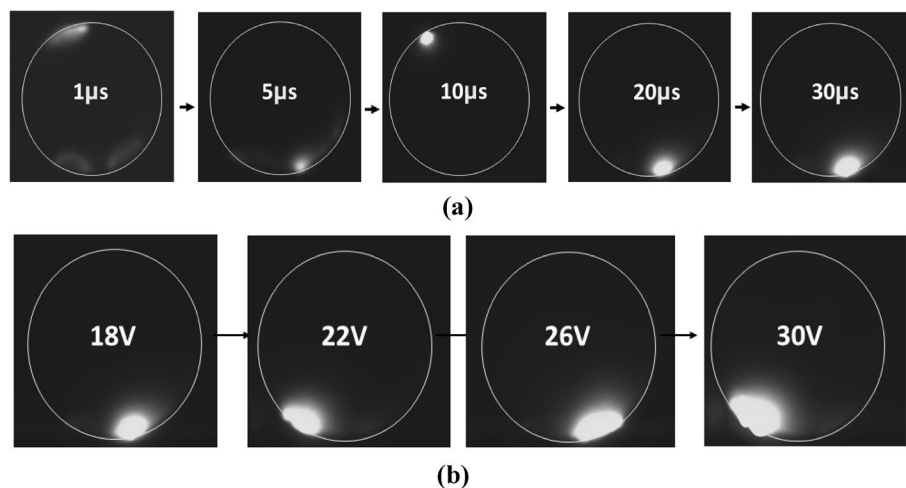

(a)

(b)

Fig. 7 **a** ICCD camera images for bright cathode/arc spots can be seen at 0.05 Torr pressure, 1 Hz pulsing frequency, 620 μs pulse width, and 18 V PPU voltage for various camera exposure times. The grey circle represents a front view of the circular arc source. **b** The camera exposure time was fixed to 30 μs and snapshots were obtained at 18, 22, 26, and 30 V PPU voltage. The high-intensity region is the cathode spot whereas the lighter region surrounding the spot is the arc region (frequency and pressure were the same)

current causes spots to be closer. Furthermore, strong coupling could lead to resistive heating in the presence of a magnetic field normal to the current direction. With further increases in PPU voltage and pulse width, the spot size may increase and form a large plasma region. In Fig. 7a for 1 μs exposure time, the arc appears to be following the trajectory of the magnetic field contours (previously simulated in "Addition of axial magnetic field" section). While, for an ideal situation/vacuum, the magnetic field would lead to the rotation of the cathode spot [2], in this case, spots can occur predominantly in the low-resistance regions (between cathode and anodes). This phenomenon is also dependent on the accuracy of part manufacturing for the CAES.

The effect of external parameters such as pulsing frequency and pressure is illustrated in Fig. 8. Additional spots can form by enlargement or division of the original cathode spot. The magnetic field at the cathode interface causes the separation distance between cathode spots to increase, as observed in Fig. 8a-c (especially at 10 Hz). The increase in gas flow (increase in pressure) squeezes the cathode spot towards the cathode interface due to the aerodynamic force generated by the incoming airflow. An instantaneous arc spot (di/dt) rate formation increases with frequency while an arc spot is not fully charged in one area. This leads to the formation of multiple spots, as observed in Fig. 8a-c for the
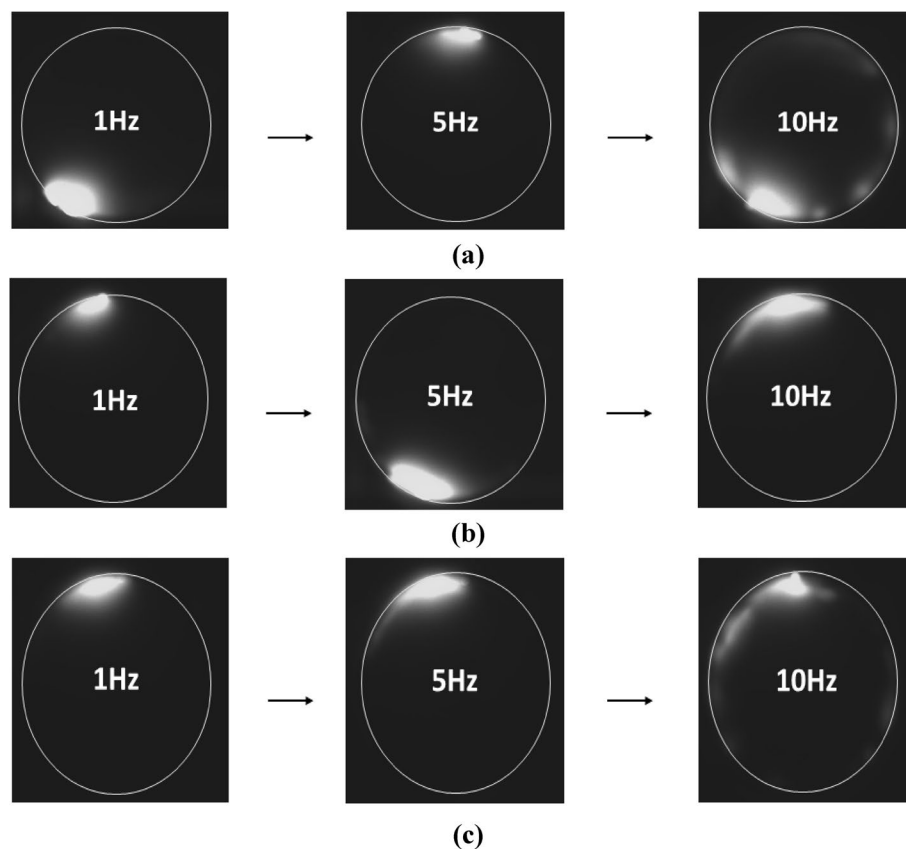

Fig. 8 ICCD camera images for bright cathode/arc spot for 0.05 (**a**), 0.07 (**b**), and 0.09 (**c**) Torr pressure, respectively, for 1, 5, and 10 Hz pulsing frequency, 620 μs pulse width, and 30 V PPU voltage at 30 μs camera exposure time. The grey circle represents a front view of the circular arc source. The high-intensity region is the cathode spot whereas the lighter region surrounding the spot is the arc region. The spreading of the cathode arcs into multiple spots can be observed at 10 Hz in all cases

10 Hz case, although discharge/arc current was not affected significantly by the change in frequency. The coupling between cathode spots can affect plasma conditions and plasma chemistry. Studying the effects of coupling between the cathode spots on plasma chemistry would require further in-depth analyses, which are beyond the scope of this research.

The effect of parameters such as pulse width and pressure are presented in Fig. 9. Experiments were performed at PPU voltage, pulse frequency, and camera exposure time of 18 V, 1 Hz, and 30 μs, respectively. At 0.05 Torr pressure, the circular shape of the cathode spot remains similar for all pulse widths as no external gas is introduced into the chamber (base pressure). For pressures greater than 0.05 Torr, an increase in the PPU pulse width led to an increment in discharge current and an increase in spot size/intensity. Like the conditions of Fig. 8, an increase in pressure leads to the splitting and compression of the cathode spot due to aerodynamic force. At higher pressures (beyond 1 Torr), the plasma density is low (high recombination), causing the camera to mostly capture a small cathode spot (less area of arc/plasma region) of the circular arc source. Additionally, the intensities of emissions are presented in Fig. 10 below.

Interestingly, the cathode spot's shape may depend on the ionization degree for the air+cathode-generated plasma. Although the quantitative analysis of cathode spot size can be challenging, the ICCD camera technique does provide qualitative insight. The effect of external parameters such as pulse width, frequency, and pressure can be observed in Fig. 10. Intensity appears to increase with PPU voltage (due to an increment in discharge current), as previously depicted in Fig. 7b. A high camera exposure window leads to a high density of photons entering from the arc into the ICCD camera, causing higher intensity spots. It was difficult to make observations for a frequency greater
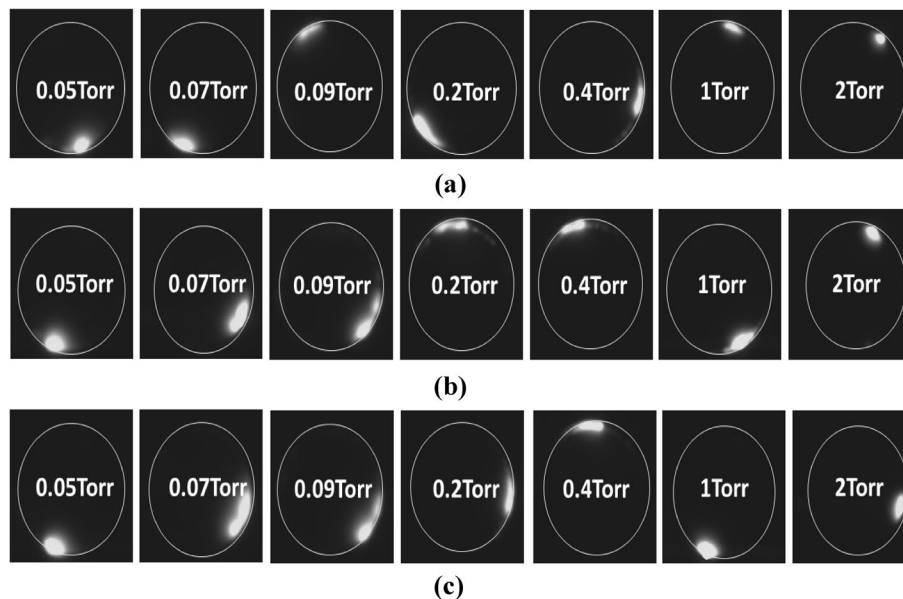

Fig. 9 ICCD camera images for bright cathode/arc spots at 620 (**a**), 820 (**b**), and 1020 μs (**c**) circular arc source's pulse width in the pressure range 0.05–2 Torr for 1 Hz pulsing frequency, 18 V PPU voltage and 30 μs camera exposure time. The grey circle represents a front view of the circular arc source. The high-intensity region is the cathode spot whereas the lighter region surrounding the spot is the arc region. Compression of the cathode spot can be observed as the pressure is increased up to 1 Torr in all cases
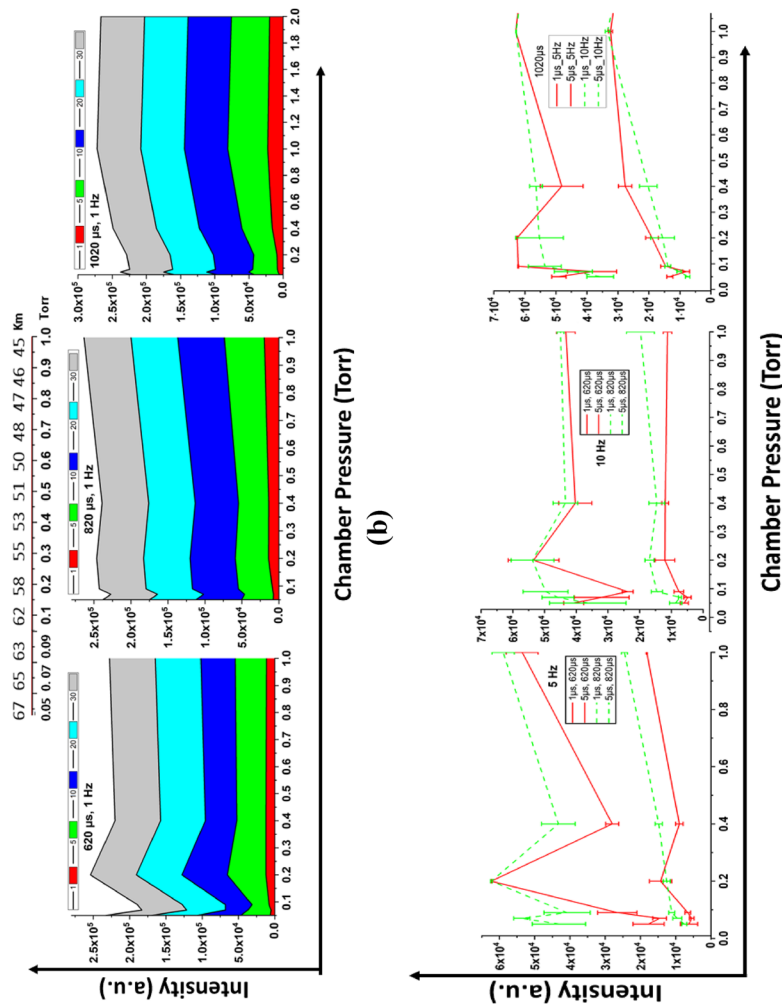
Fig. 10 a Maximum arcing intensity (with standard deviation) using an ICCD camera varying with PPU voltage (18–26 V), pressure (0.05–0.09 Torr) at 1 Hz pulsing frequency, and 1–10 μs camera exposure time can be seen. **b** The maximum arcing intensity area map vs pressure (0.05–2 Torr) for pulse width 620–1020 μs at 1 Hz pulsing frequency, 30 μs camera exposure time, and 18 V PPU voltage can be observed. The scale of pressure vs. the corresponding altitude was obtained by converting pressure to neutral density and comparing it with altitude [37]). **c** Lastly, maximum arcing intensity (with standard deviation) variation with pressure (0.05–1 Torr), pulse width (620–1020 μs), and pulsing frequency (5, 10 Hz) can be seen at 1 and 5 μs camera exposure time

than 5 Hz due to instantaneous cathode spot generation at larger PPU voltages (higher arc currents). Maximum peak emission intensity was observed in the case of 26 V PPU voltage using the ICCD camera technique. The S pattern observed for 0.07–0.2 Torr is unknown but could be the result of a resonance effect occurring between arc plasma and the air plasma generated by it. This pattern is observed at different pulse widths and frequencies. In Fig. 10c, the peak intensity occurring near 0.1–0.2 Torr (620 μs, 5 and 10 Hz) could be due to the arc voltage reaching close to the Paschen curve limit [18]. At a pulse width of 1020 μs, the plasma/arc current became unstable. The pressure range shown above (Fig. 10b) corresponds to an altitude range of 45–67 km. The CAES's operation in high pressure creates opportunities for air-breathing plasma propulsion capabilities in VLEOs. Earlier, we described CAES as consisting of a circular arc source and an electron extraction grid. The grid may undergo depositions and loss in conductance due to its operation in harsh plasma environments. In the next section, we studied the deposition and the conductance of the grid using SEM and CMS.

Deposition thickness and conductance analysis

The CAES's electron extraction grid would experience harsh plasma environments in VLEO. SEM images corresponding to before and after long operation of the CAES's electron extraction grid are shown in Fig. 11. Here, SEM was used to study both the deposition quantity and quality. The procedure involved the creation of small sections of the aluminum grid sample. The grids were cut into smaller pieces using a pair of scissors. The sections were first carefully placed on a stub with carbon tape and left in the desiccator for two hours during the venting and purging process of the SEM.

The grid samples that were exposed to an air plasma environment show a higher roughness of the surface and some deposition that is visible compared to the unexposed grid samples (Fig. 11), where about the same magnification is used. The images were taken at three magnifications 100x, 500x, 1000x, and 12000x, respectively, as shown in Fig. 11a and d. The grid thickness control vs. deposition was analyzed by using ImageJ [38]. The measurements were performed by calibrating the images in ImageJ concerning its scale bar. The snapshots were acquired in a high vacuum with a voltage of 5.00 kV and a current of 0.2 nA using a secondary electron and back-scattered electron detector called the Everhart–Thornley detector (ETD) [39]. The electron extraction grid sample images at various magnifications were obtained using SEM. The image at 100x (Fig. 11a) shows significant deposition in the cross's center and inner regions. Increments in the magnification at 500x (Fig. 11b), 1000x (Fig. 11c), and 12000x (Fig. 11d), revealed innumerable microgranular structures due to depositions. Figure 11b and c show (marked with a red circle) the control aluminum grid vs. exposed surface hiding under micro

(See figure on next page.)
Fig. 11 Grid sample images with and without deposition obtained using SEM. The cut section top view control vs. deposition sample (**a**) at 100 × magnification were compared. Simultaneously, control vs. deposition samples at 500 (**b**), 1000 (**c**), and 12000x (**d**) magnification were compared. The red circle in the images is believed to be a region of major deposition, primarily from the cathode material of the CAES. Additionally, deposition is compared for a side view cut section (**e**) of the grid sample at 200 × magnification vs. control. (**e**) The red circle is believed to be a region of powdered deposition that chipped off from the sample during preparation
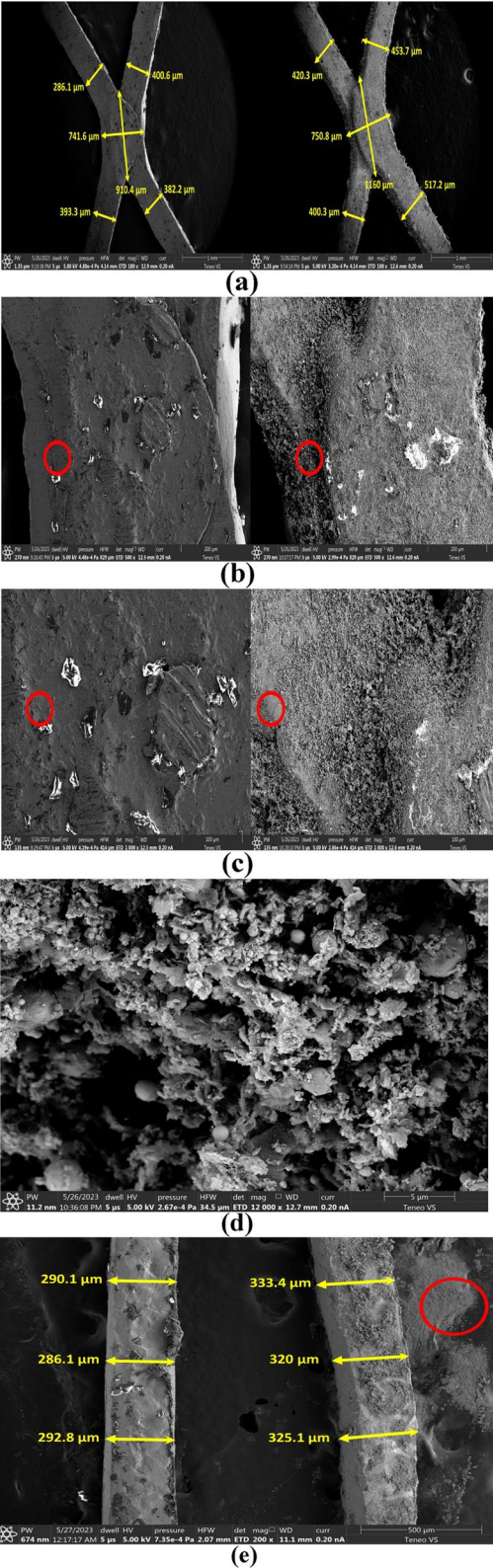
Fig. 11 (See legend on previous page.)

depositions. The inner sections (Fig. 11a) are sharp areas of high electric field regions where high-energy electrons from arc plasma would pass and lead to secondary electron emission. In contrast, on the top, there was an almost uniform deposition layer. The electron extraction grid had deposition on both sides, indicating that the grid was subjected to extreme air plasma environments. Indeed, it is also crucial to note that the deposition was amorphous/granular, as indicated by the red circle in Fig. 11e. Figure 11a and e show significant deposition on the grid material (control vs. treated). Six arbitrary positions in the material were selected to obtain the total accumulation thickness. For the region shown in Fig. 11a and e, the total accumulation (summation $\Sigma_{\text{deposited}} - \Sigma_{\text{control}}$) is estimated to be 588.1 (~ 600) and 110 µm, respectively. With the increase in the deposition, the conductance of the grid was diminished.

To study conductance, a clean aluminum grid (control) without any deposition was first measured using the CMS method. Then, the AES assembly (arc source and the grid [2]) was placed inside the plasma chamber with a bias of 0 V on the grid. The AES was then operated at 20-min intervals for 80 min total. Between each interval, the AES was taken out to obtain an I-V curve using CMS. The same method was repeated for another control grid but with a 300 V bias (on the grid) applied instead. An ordinary least squares regression was performed on each I-V curve to determine the value of the conductance as the slope of the line $I \sim \sigma V$ (current $\sim$ conductancetimesvoltage). By repeating this procedure for each voltage and time-point, the conductance data was obtained as a function of time, as shown in Fig. 12, where it is plotted for each grid sample. It was observed that each sample exhibited an initial increase in conductance, with the 0 V
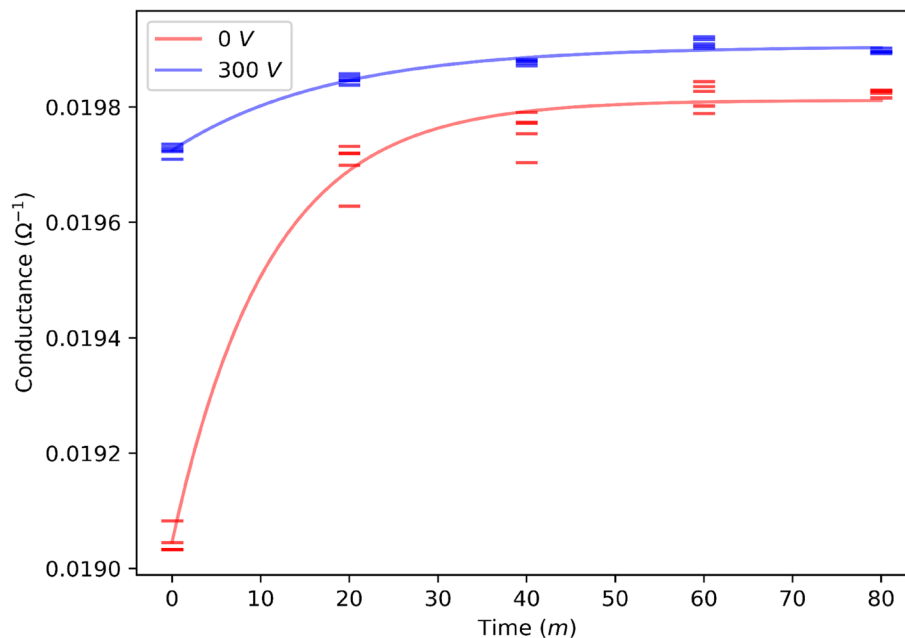

Fig. 12 Conductance values calculated from sets of I-V curves vs. time, color-coded according to voltage: red for 0 V and blue for 300 V. The values calculated at specific instants are shown as horizontal, rectangular markers. We fit a saturating exponential growth model to the data (solid lines) which indicates an interplay between an increasing conductance due to deposition and a potentially diminishing deposition layer thickness

sample increasing the most drastically and in the shortest time. The 300 V sample follows a similar trend, with an increase in growth rate in the same order as the 0 V sample, but through a smaller range. A temporary carbon deposition due to carbon paint may have a transient effect on the conductance. Although the deposition on the grid may be due to carbon and the cathode material, we postulate that the increase in conductance is primarily due to the cathode material from the coaxial arc source [2]. However, more testing is needed to fully elucidate this process.

Furthermore, we observe that the data closely follow a saturating exponential, suggesting an interesting competition between a driving force and a dissipating force. The saturation in the thickness of the deposited layer could account for such dynamic behavior. We describe the data with a model of the form.

$$\sigma(t) = \sigma_0 + (\sigma_\infty - \sigma_0)(1 - exp(-t/\tau)) \tag{1}$$

Here, σ_0 is the base conductance of the grid assembly before the deposition, σ_∞ is the value of the conductance achieved after saturation, and τ is the time constant of the transition between the two conductance values. The SABPT [1, 2] would operate by controlling the mean electron energy (controlling bias on the grid) of the CAES to produce positive and negative ions in harsh plasma environments. The continuous operation of the thruster may prevent the conductance from dropping, thereby creating an electrically "self-healing electron extraction grid material".

Concluding remarks

This study aimed to characterize a magnetically enhanced CAES and coaxial AES [2] for air ionization applications inside an SABPT. It was designed using a circular vacuum arc plasma source coupled with an electron extraction grid like the previously proposed AES [2]. The grid-enabled the control of the mean electron energy. Experimentally, it was shown that the positive ion current density and electron density increased with an increment in the grid voltage, whereas the negative ion current density dropped as a function of grid voltage due to electron detachment. In comparison with AES [2], CAES produced higher electron density while exhibiting lower sensitivity to pressure. The ICCD camera technique provided a qualitative analysis of the cathode spot/air plasma region, revealing a peak emission intensity in the case of 26 V PPU voltage. Prolonged exposure to harsh plasma environments resulted in the deposition of approximately 600 and 110 microns on the sample's front and side cut sections, respectively (deposition could lower electrical conductance). Surprisingly, the conductance of the grid increased and eventually saturated, thereby making the grid electrically "self-healing". The ability of the electron extraction grid to electrically "self-heal" over time would extend the lifetime of the SABPT-powered spacecraft/satellite. Furthermore, a combination of the current probe, ICCD camera technique, SEM, and CMS diagnostics facilitated the characterization of the CAES and coaxial AES [2].

The mechanism of SABPT involves alternating the mean electron energy of an electron source to create positive and negative ions to achieve self-neutralization [1, 2]. The maximum ion current densities and electron densities were 8.06×10^2 Am^{-2} (positive), 1.8×10^2 Am^{-2} (negative), and 1.62×10^{18} m^{-3} for 0.05 Torr pressure. The experimental results suggest that conditions for the self-neutralizing air-breathing plasma thruster

proposed theoretically can be achieved with the improved CAES. While the air inlet is positioned to align with the central hole of CAES, it has not been designed or tested since it is outside the current research's focus. The potential to operate at a pressure of up to 6 Torr may also enable SABPT-built spacecraft/satellites to operate at very low altitudes, as hybrid air-breathing electric engines in the future. Additionally, machine learning-based system control algorithms [40, 41] could be used to have more precise control over plasma chemistry in the thruster. Further scaling up of the system in power and size is necessary to generate thrust for very low earth orbit applications.

Authors' contributions
The first draft of the manuscript was written by AT. AT performed experiments and analysis for the current probe and magnetic filter ("Addition of axial magnetic field" and "Plasma parameters" sections), ICCD camera technique ("ICCD High-Speed Camera Experiments" and "Arc rotation" sections), and electron extraction grid plasma treatment in the plasma chamber ("SEM and conductance measurements" and "Deposition thickness and conductance analysis " sections). VS performed SEM sample preparations and experiments and contributed to SEM theory ("SEM and conductance measurements" section) and imaging/analysis ("Deposition thickness and conductance analysis " section). HS and MM contributed to CMS theory ("SEM and conductance measurements" section) and analysis ("Deposition thickness and conductance analysis " section). LL assisted with the ICCD camera measurements ("ICCD High-Speed Camera Experiments" section). JS performed magnet simulations ("Addition of axial magnetic field" section). Supervision: MK and SS, and project administration: MK. All authors provided comments/revisions to the manuscript. AT made corrections to the manuscript.

Availability of data and materials
The datasets generated during and/or analyzed during the current study are available from the corresponding author upon reasonable request.

Declarations

Consent for publication
All authors gave their explicit consent to submit the content of this article for publication in the Springer Journal of Electric Propulsion.

Competing interests
The authors declare no competing interests.

References
1. Taploo A, Lin Li, Keidar M (2021) Analysis of ionization in air-breathing plasma thruster. Phys Plasmas 28:093505. https://doi.org/10.1063/5.0059896
2. Taploo A, Lin L, Keidar M (2022) Air ionization in self-neutralizing air-breathing plasma thruster. J Electric Propulsion 1:25. https://doi.org/10.1007/s44205-022-00022-x
3. Ferrato, Giannetti, Piragino, Andrenucci and Andreussi, Development Roadmap of SITAEL's RAM-EP System, (2019). http://electricrocket.org/2019/886.pdf
4. Pekker L, Keidar M (2012) Analysis of Airbreathing Hall-Effect Thrusters. J Propul Power 28:1399. https://doi.org/10.2514/1.B34441
5. Andreussi et al (2022) A review of air-breathing electric propulsion: from mission studies to technology verification. J Electric Propuls 1:31. https://doi.org/10.1007/s44205-022-00024-9
6. A.S. Gilmour and D.L. Lockwood, "Pulsed metallic-plasma generators". IEEE Xplore. (n.d.). Retrieved January 27, 2022, from https://ieeexplore.ieee.org/abstract/document/1450751
7. Michael Keidar, Jochen Schein, Kristi Wilson et. al. "Magnetically enhanced vacuum arc thruster" - iopscience. (n.d.). Retrieved January 27, 2022, from https://iopscience.iop.org/article/https://doi.org/10.1088/0963-0252/14/4/004
8. Zhuang T, Shashurin A, Denz T, Keidar M, Vail P, Pancotti A (2014) Performance characteristics of micro-cathode Arc Thruster. J Propuls Power. 30(1):29–34. https://doi.org/10.2514/1.b34567
9. USNA, "BRICSAT-P - satellite missions" - eoportal directory. P. (n.d.). Retrieved January 27, 2022, from https://www.eoportal.org/satellite-missions/bricsat-p#eop-quick-facts-section

10. Zolotuchin D B, Banduru R S P, Daniels K P, Beilis I I, Keidar M (2022) Demonstration of electric micro-propulsion multimodality. Sci Adv 8:eadc9850

11. Keir P. Daniels, "Lifetime investigations of micro-cathode and Matrix Arc Thrusters". Pg. 105 (n.d.-a). https://www.proquest.com/openview/836c07a48488c0727a038a39d2470dce/1?pq-origsite=gscholar&cbl=18750&diss=y

12. A. Aanesland, D. Rafalskyi, J. Bredin et. al., "The PEGASES gridded ion-ion thruster performance and predictions". Electric Rocket Propulsion Society - Home. (n.d.-b). http://electricrocket.org/IEPC/mccl88wv.pdf

13. D. Gerst, D. Renaud, S. Mazouffre et. al. « E×B probe investigation of the PEGASES thruster ion beam in Xe and SF_6". Electric Rocket Propulsion Society - Home. (n.d.). http://electricrocket.org/IEPC/e31m2jx0.pdf

14. Aanesland A, Meige A, Chabert P (2009) « Electric propulsion using Ion-Ion Plasmas". J Phys: Conf Ser 162:012009. https://doi.org/10.1088/1742-6596/162/1/012009

15. Aanesland, A., Bredin, J., Popelier, L., & Chabert, P. (2014, November 6). "Direction for the future - successive acceleration of positive and negative ions applied to space propulsion". arXiv.org. https://arxiv.org/abs/1411.1538

16. Rafalskyi D, Aanesland A (2016) Brief review on plasma propulsion with neutralizer-free systems. Plasma Sources Sci Technol 25:043001. https://doi.org/10.1088/0963-0252/25/4/043001

17. Munro JJ, Harrison S, Fujimoto MM, Tennyson J (2012) A dissociative electron attachment cross-section estimator. J Phys Conf Ser. 388:012013. https://doi.org/10.1088/1742-6596/388/1/012013

18. Martins, A., & Pinheiro, M. (2011, October 01). "On the propulsive force developed by asymmetric capacitors in a vacuum". https://doi.org/10.1016/j.phpro.2011.08.010

19. Lun, J. (2009). "Development of a vacuum arc thruster for nanosatellite propulsion". pp. 4–6, http://hdl.handle.net/10019.1/1527

20. Switzer. (1970, January 1). "Development and characterization of the Capacitive Power Processing Unit (CPPU) for the Micro-Cathode Arc Thruster". GW ScholarSpace. Pg. 74, https://scholarspace.library.gwu.edu/concern/gw_etds/n009w296m

21. Rysanek, F., Hartmann, J., Schein, J., & Binder, R. (1970, January 1). "Microvacuum arc thruster design for a CubeSat class satellite": Semantic scholar. undefined. Retrieved January 27, 2022, from https://www.semanticscholar.org/paper/Microvacuum-Arc-Thruster-Design-for-a-Cubesat-Class-Rysanek-Hartmann/1a47b6e7ffc9ecc1926b3db0de121743ef08d280

22. 33220A agilent function generator. ValueTronics International. (n.d.). https://www.valuetronics.com/product/33220a-agilent-function-generator-used

23. Zolotukhin DB, Keidar M (2018) Optimization of discharge triggering in micro-cathode vacuum arc thruster for CubeSats. Plasma Sources Sci Technol 27:074001. https://doi.org/10.1088/1361-6595/aacdb0

24. Istar 334t CCD - andor. Oxford Instruments. (n.d.). https://andor.oxinst.com/products/intensified-camera-series/istar-334t

25. The AC/DC Module User's Guide - COMSOL MULTIPHYSICS. (n.d.-d). Pg. 269–277 https://doc.comsol.com/5.4/doc/com.comsol.help.acdc/ACDCModuleUsersGuide.pdf

26. KJmagnetics. K&J Magnetics - Demagnetization Curves. (n.d.). https://www.kjmagnetics.com/bhcurves.asp

27. Methling R, Popov SA, Batrakov AV, Uhrlandt D, Weltmann K-D (2013) Spectroscopy of single vacuum arc cathode spots with improved sensitivity. IEEE Trans Plasma Sci 41(8):1904–1910. https://doi.org/10.1109/tps.2013.2253131

28. B. Juttner, "Nanosecond displacement times of arc cathode spots in a vacuum." (n.d.-b). https://ieeexplore.ieee.org/document/782247/

29. Xia W-D, Zhou H-L, Zhou Z-P, Bai B (2008) Evolution of cathodic arc roots in a large-scale magnetically rotating arc plasma. IEEE Trans Plasma Sci 36(4):1048–1049. https://doi.org/10.1109/tps.2004.924569

30. Wang C, Li J, Zhang Z et al (2019) An Experimental Investigation of Cathode Spot Motion in a Magnetically Rotating Arc Plasma Generator at Atmospheric Pressure. Plasma Chem Plasma Process 39:259–276. https://doi.org/10.1007/s11090-018-9937-8

31. WAVETEK 166 pulse generator 50 MHz 3AG 250V (66050 - used). SIGMA Surplus. (n.d.). https://sigmasurplus.com/wavetek-166-pulse-generator-50-mhz-3ag-250v/

32. Nikon 55mm f/2.8 ai-S. (n.d.). https://www.kenrockwell.com/nikon/55f28ais.htm

33. Fei Teneo LV SEM: GW Nanofabrication & Imaging Center: The George Washington University. GW Nanofabrication & Imaging Center. (n.d.). https://nic.gwu.edu/fei-teneo-lv-sem

34. Variable Gain Low Noise Current Amplifier. Femto. (n.d.). https://www.femto.de/en/products/current-amplifiers/variable-gain-up-to-500-khz-dlpca/33-variable-gain-low-noise-current-amplifier-dlpca-200.html

35. SDS1052DL+. Siglent. (2023, July 5). https://siglentna.com/product/sds1052dl-2/

36. Beilis I.I. Plasma and Spot Phenomena in Electrical Arcs, Pg. 1113 . Switzerland, AG, Springer Nature, volumes 1 and 2, 2020

37. MSISE Earth model database (4See https://ccmc.gsfc.nasa.gov/modelweb/models/msis_vitmo.php for "MSIS-E90 Atmosphere Model," (2022)

38. U.S. Department of Health and Human Services. (n.d.). ImageJ. National Institutes of Health. https://imagej.nih.gov/ij/download.html

39. Everhart–thornley detector. DBpedia. (n.d.). https://dbpedia.org/page/Everhart%E2%80%93Thornley_detector

40. Lin L, Keidar M (2022) Artificial Intelligence without Digital Computers: Programming Matter at a Molecular Scale. Adv Intell Syst 4:2200157. https://doi.org/10.1002/aisy.202200157

41. Corless, V. (2022, October 27). "AI without computers". Advanced Science News. https://www.advancedsciencenews.com/ai-without-computers/

Publisher's Note